



Synthesis and Characterization of $\text{Ti}_{50}\text{Ni}_{(50-x)}\text{Fe}_x$ Alloy Produced by Mechanical Alloying and Pressure-Less Sintering

Jagadish Parida¹ · Subash Chandra Mishra¹ · Ajit Behera¹

Received: 25 March 2022 / Accepted: 13 July 2022 / Published online: 11 December 2022
© The Author(s) under exclusive licence to The Korean Institute of Metals and Materials 2022

Abstract

This paper investigated the effect of iron on the $\text{Ti}_{50}\text{Ni}_{(50-x)}\text{Fe}_x$ alloy fabricated by the powder metallurgy method. The different powder compositions are prepared by planetary ball milling for 8 h, then compacted at 600 MPa and sintered at 1050 °C for 4 h. Microstructure, chemical composition, and phase evolution of powder and sintered sample were investigated by SEM, EDS, and XRD. Also, the density, hardness, wear, compressive strength, and shape memory effect was measured for each of the sintered samples. SEM and XRD analysis show that sintered sample consists of the (Ni, Fe)-rich and Ti-rich phases with some pores. Porosity has a major effect on the decreases in hardness, density, and compression strength. The lower coefficient of friction, maximum relative density, and higher hardness of 0.37, 66.31%, and 372.7VHN respectively was observed in the 8Fe contained sample but maximum yield strength and compression strength of 67.66 MPa and 76.16 MPa respectively are found without iron sample than other composition samples. The intermetallic secondary phase formation helps improve the hardness and wear properties, but the presence of martensite (NiTi) phase helps higher strength and shape memory effect values of the alloy. Abrasive wear mechanism obtained from SEM analysis of the worn surface of all wear samples.

Keywords TiNiFe alloys · Mechanical alloying · Pressure-less sintering · Intermetallic compound

1 Introduction

Shape memory alloys (SMAs) shows crystal structure transformation at low temperature. Due to this reason, the metals change their shape without any microstructure affect. Also, SMAs exhibit superior properties like excellent pseudoelasticity, biocompatibility, corrosion resistance, and processability, etc. [1–3]. NiTi-based alloys with shape memory effect (SME) are used in different areas such as electronics, medicine, aerospace, robotics, and structural applications [4–6]. Among them, the TiNiFe ternary alloys are the SMAs, which show good mechanical properties and high corrosion resistance at elevated and low temperatures. These alloys are very useful for the power industry due to the financial profits: for example, the long life of the electric turbines and power plants whereas other elements under very destructive conditions (i.e., high-temperature corrosion) in comparison

to the use of other traditional materials [7]. TiNiFe alloys are mostly used in aeronautical (for example heat-shrinkable hydraulic couplings and sleeves) and other engineering applications (like hydrogen storage materials etc.) [8, 9].

Based on the literature, the $\text{Ti}_{50}\text{Ni}_{50-x}\text{S}_x$ ($\text{S} = \text{Cu}, \text{Fe}, \text{Co}$, and $x < 25\%$) ternary alloy is a solid solution of S in a NiTi alloy, with Ni replaced by S atoms [7, 10, 13]. The NiTi alloys are monoclinic (B19') structures (i.e., the martensitic phase) at room temperature. The B19' transforms to hexagonal/trigonal (B19) phase (i.e., pre-martensitic or R phase) and then transforms into a cubic (B2) structure (i.e., austenitic phase) by increased temperature. The reverse transformations $\text{B2} \rightarrow \text{B19} \rightarrow \text{B19}'$ are obtained when cooled from high temperatures. Sometimes $\text{B19} \leftrightarrow \text{B19}'$ transformation occurs at a temperature where low enough to inhibit diffusion-controlled process; it is called diffusion-less phase transformations (i.e., Martensitic transformations) [7, 10]. The phase transformation temperatures and functional properties of the alloys are changed by the addition of a third alloying element. TiNiFe shows two-stage phase transformation behaviour i.e., $\text{B2} \rightarrow \text{R} \rightarrow \text{B19}'$ without any additional thermomechanical treatment. In other words, it produces rhombohedral an R-phase intermediate between

✉ Ajit Behera
beherajit@nitrkl.ac.in

¹ Department of Metallurgical and Materials Engineering,
National Institute of Technology, Rourkela, Odisha 769008,
India

the martensite and austenite [11], the temperature range between the B2 and the R-phase offers a practical temperature limit for actuator applications as the material shows a low-temperature hysteresis with desirable fatigue properties because of R-phase transformation [12].

TiNiFe alloys are produced by different techniques, including vacuum induction melting [10, 13], mechanical alloying (MA) [12, 14, 15], and powder metallurgy [16]. As per the literature, MA is the low-cost and simple solid-state process for achieving non-equilibrium states i.e., consists of amorphous phases, nanostructured materials, and supersaturated solid solutions. During the MA process, powder particles undergo severe plastic deformations and large extents of defects are created. The main purpose is to get a homogeneous structure that results in an enhancement of properties.

The powder metallurgy route gives some advantages, such as (1) thermomechanical treatment is not required but it is necessary after conventional casting process, and (2) VIM and VAR processes are required for several times to make homogeneity of ingots and are responsible for higher production cost. However, it produces pore, which diminishes mechanical properties. A modern alternative to these melting routes is powder metallurgy, which promises to produce pure materials. Many methods are used for sintering i.e., solid or liquid phase sintering, cold or hot isostatic pressing, and plasma sintering. A simple non-conventional powder metallurgy production method is pressure-less sintering [17].

The study on the wear behavior of NiTi-based alloys as compared to other materials such as Ni-based, steels, and various high-grade stellite alloys has been investigated [17–19]. These results indicate that NiTi-based alloy is higher wear resistance compared with other tribological materials. The dry conditions sliding wear of NiTi alloy are studied and it is found that this alloy was about 10–30 times higher wear resistance than pure Ti and Ni metal [20]. TiNiFe ternary alloys exhibit good wear resistance under conditions of sliding/rolling contact, which gives to the alloy hardening by the application of cyclic stresses during the sliding wear process [18]. However, only a few studies are done to understand the wear behaviour of TiNiFe alloys.

In the literature, few studies are done on TiNiFe alloys from elemental powders by MA. Nanoscale $Ti_{50}Ni_{40}Fe_{10}$ powder is produced by MA in a rotating ball mill with a 20:1 ball-to-powder (BPR) weight ratio and 110 RPM rotational velocity for 400 h in an argon atmosphere [15]. It is found that crystallite size decreased with the milling time increases based on Williamson-Hall and Scherrer's methods. The crystallite size and lattice internal strain values are 2.4 nm and 3.19×10^{-3} respectively for milling 300 h. The $NiTiO_3$, $FeNi_3$, and TiO_2 peaks are observed from XRD analysis after 1000 °C annealing. Another study carried out by Ferreira et al. [14] reports on the $Ti_{50}Ni_{25}Fe_{25}$ phase (i.e.B2) that

formed by MA under argon atmosphere at room temperature for 8 h with a 5:1 BPR weight ratio. It is found that the amorphous phase was formed and the B2 phase was obtained up to 7 GPa but the B2 transformed into a B19 phase for the 18 GPa pressure used. Apart from B2 and B19, free Ni or γ -(Fe, Ni) and $FeNi_3$ were also obtained.

Several researchers study TiNiFe alloys with different variations of Fe % by casting routes but only a few studies are done based on this composition by powder metallurgy routes. The novelty of our research work is to find out, the effect of iron (Fe) additions in $Ti_{50}Ni_{(50-x)}Fe_x$ which is produced by the powder metallurgy route. The fabricated ternary alloy was sintered at 1050 °C for 4 h under an argon gas atmosphere. The phase evolution, microstructure, chemical composition, and properties of TiNiFe alloys with a composition of $Ti_{50}Ni_{50-x}Fe_x$ ($x=0, 2, 4, 6, 8$, and 10 at%) have been investigated using XRD, SEM, EDS, shape memory effect (SME) and mechanical tests (hardness measurement, wear test, and compression test).

2 Experimental Procedures

2.1 Materials Used

In this research work, elemental titanium, nickel, and iron powders were used to make TiNiFe (at%) alloys by powder metallurgy method, which consists of mixing, milling, compacting, and sintering processes. The powder's details (i.e., purity, particle size, and origins of powder used in this experimental work) are shown in Table 1.

2.2 Preparation of Samples

Each of the metal powders was weighed and mixed in a Turbula shaker mixer (Willy A. Bachofen AG, Maschinenfabrik, Switzerland) for 12 h in order to get a homogeneous mixture according to compositions of $Ti_{50}Ni_{50-x}Fe_x$ ($x=0, 2, 4, 6, 8$ and 10 at%) shown in Table 2. Then mixed powders were mechanical alloyed in a dry condition at room temperature in the Ar-atmosphere (to avoid nitrogen/oxygen contamination from the atmosphere). Mechanical alloying experimental parameter details are investigated in Table 3 [20]. To avoid increased temperature inside vial during MA, 15 min milled

Table 1 Purity and Particle size of Ni, Ti, and Fe powder

Metal powder	Purity (%)	Particle size (μm)	Source
Ni	99.8	– 150 + 200 mesh (74–100 μm)	Alfa Aesar
Ti	99.5	– 325 mesh (45 μm)	Alfa Aesar
Fe	99.5	6–10 μm	Alfa Aesar

Table 2 Composition of alloy for experimental work

Sample code	Sample name	Composition (atomic %)		
		Nickel	Titanium	Iron
0Fe	50Ni50Ti	50	50	0
2Fe	48Ni50Ti2Fe	48	50	2
4Fe	46Ni50Ti4Fe	46	50	4
6Fe	44Ni50Ti6Fe	44	50	6
8Fe	42Ni50Ti8Fe	42	50	8
10Fe	40Ni50Ti10Fe	40	50	10

than stop 15 min then start and vice-versa. The milling was interrupted after 4 h to collect powder in small quantities for SEM–EDS and XRD analyses for known changes in powder morphology. The particle size analyzer is used to measure milled powder particle size by laser diffraction technique (Model: S3500 and Make: Microtrac, USA).

After milling, the powders are compacted in a uniaxial cold pressing with 600 MPa pressure (i.e. 4.8 Ton load) for 4 min at room temperature (no lubricants are used making pellet during compaction because it may be produced impurities during sintering) and then compacted samples (cylindrical shape green pellet) were pressure-less sintered at temperature 1050 °C for 4 h time in a tubular furnace with heating and cooling rate of 5 °C/min under an argon atmosphere (purity: 99.99% and constant injection rate: 100 ml/min) followed by furnace cooling. The sintering temperature 1050 °C which is higher than lowest temperature (942 °C) liquidus line in binary Ni–Ti phase diagram and it lower temperature than lowest temperature (1085 and 1443 °C) on liquidus line in binary Fe–Ti and Fe–Ni phase diagram.

2.3 Characterization and Mechanical Testing of a Samples

After milling, the milled powders were characterized by scanning electron microscopy (JEOL JSM-6480 LV) equipped with energy dispersive spectroscopy (EDS)

and X-ray diffraction (BRUKER model: D8 ADVANCE XRD) using Co–K α ($\lambda = 1.789\text{\AA}$) radiation with 5°/min scan rate, 30°–100° scanning range and 0.02 step size to study the morphological changes, structural and evolution of phases during milling.

After sintering, all samples were first grinded by belt grinder and then used a series of emery paper grits (i.e., (P400) → (P800) → (P1200) → (P2000)) and finally, samples were polished in velvet cloth with diamond paste to remove scratches. Then it is stored in a desiccator for different characterization and mechanical properties study. Sintered samples were characterized for the phase evolution and micro-structure analyzing by XRD (30–120° scanning range) and SEM–EDS. The hardness value of samples was measured using a Vickers hardness tester (Leco LM248AT). Taken ten no's indentations (to get the average value) for each sample with a varying load of 100–500 gf and indentation time of 10 s [21]. The compression test has done at room temperature using a universal testing machine (Instron SATEC KN600) with a strain rate of 0.1 mm/min and dimension ratio of H/D more than 0.8 according to ASTM standard E28: E9-09 for a small sample. The wear test of samples was measured by a ball-on-plate wear tester (Make: Ducom, Model: TR-208-M1) in Si₃N₄ ceramic ball under 10 N load with sliding speed of 30 rpm and 10 min time respectively [19, 22]. The shape memory effect is calculated by indentation technique using the Vickers hardness tester at room temperature with an applied load of 1 kg-f for 10 s. After that, the sample is heated up to 100 °C, held for 30 min in a vacuum furnace and cooled in a vacuum furnace to measure the shape recovery [23].

2.4 Physical Properties of Sample

The theoretical density of the mixed powder is calculated by the weight percentages of individual powder multiply by its theoretical density as follows [16, 24]:

Table 3 MA process condition, parameters, and mills details

Rotation speed (rpm)	300
Milling Atmosphere	Argon
Ball mill type	High energy dual-drive planetary mill (DDPM)
Mill specification	Main shaft length(L): 640 mm, Main shaft speed:133 rpm, and jar speed:300 rpm Critical speed: 64%
Ball-to-powder ratio (BPR)	10:1
Milling time (h)	0–8
Process control agent (PCA)	No
Vial	Stainless steel (volume:1L and dia.: 100 mm)
Balls	Stainless steel (diameter:10 mm and quantity:103 numbers)

$$\text{Theoretical density (g/cc)} = \frac{\sum [(wt.ofTi \times densityofTi) + (wt.ofNi \times densityofNi) + (wt.ofFe \times densityofFe)]}{\text{Volumeofcompact(cc)}} \quad (1)$$

The density and porosity of compacted samples were calculated by the following equation [9, 10]:

$$\text{Green density (g/cc)} = \frac{\text{Weightofcompact(g)}}{\text{Volumeofcompact(cc)}} \quad (2)$$

$$\text{Green porosity (\%)} = \frac{\text{Theoretical density} - \text{Green density}}{\text{Theoretical density}} \times 100 \quad (3)$$

The sintered sample densities were determined by the Archimedes principle. The sintered and relative densities were calculated by the following equations [25].

$$\text{Sinter density (g/cc)} = \frac{W_1}{W_2 - W_3} \times \text{density of water} \quad (4)$$

where W_1 = mass of sinter sample in air, W_2 = mass of soaked sample in air (soaked sample means the weight of the sample after dipping in distilled water for 24 h) and W_3 = mass-soaked sample in distilled water.

$$\text{Relative density (\%)} = \frac{\text{Sinter density}}{\text{Theoretical density}} \times 100 \quad (5)$$

3 Results and Discussion

3.1 Powder Characterization

Figure 1 shows an XRD analysis and SEM image of as-received Ni, Ti, and Fe powders. From the SEM image, it is seen that Ni powder particles are regular ball-type (spherical) shapes with a mean diameter of 74–100 μm . Both Ti and Fe powder particles are irregular (angular) type shapes with a particle diameter of up to a maximum of 45 μm and 6–10 μm respectively. XRD analysis shows that the raw powder of Ni(fcc), Ti(hcp), and Fe(bcc) with reference codes 98-012-3812, 98-007-1735 and 98-008-8002 respectively. The high peak intensity of Fe and Ni than Ti in raw material because of an atomic number higher. So high scattering factor of Fe and Ni than Ti.

Figure 2a shows the amount of the recovered powder from the vial as a function of milling time. The recoverable amount of each powder after mechanical alloying decreases drastically for an alloying time of up to 8 h, and additional alloying slightly decreases the amount of recoverable powders. It is found that the powders have heavily adhered to the stainless-steel vial inner wall and balls surface during mechanical alloying because we did not use any dispersant in this study for the reduction of chemical contamination. The powders without iron (0Fe) seem to be recovered fairly better than the 10Fe powder after 8 h alloying time.

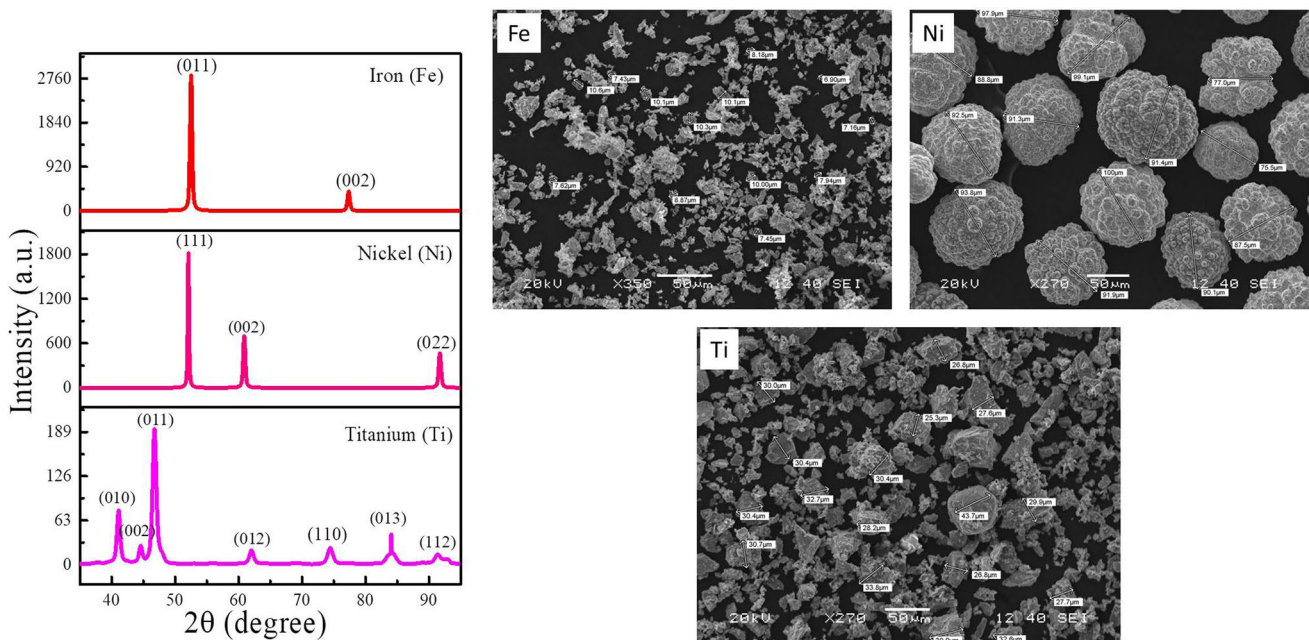


Fig. 1 XRD analysis and SEM micrographs of as received iron, nickel and titanium powders

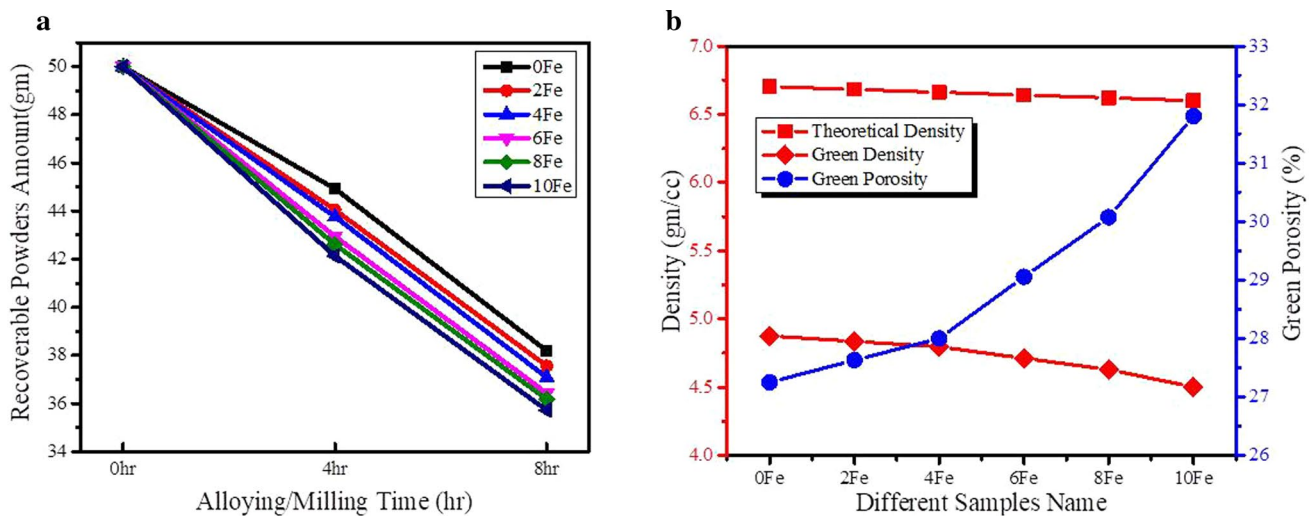


Fig. 2 **a** The recoverable powders amount after mechanical alloying as a function of alloying time and **b** Theoretical density of mixed powder, green density, and green porosity of compact powder Vs different percentages of Fe

Figure 3 shows the continuous changes in particle morphology of the milled $\text{Ti}_{50}\text{Ni}_{50-x}\text{Fe}_x$ ($x = 0, 2, 4, 6, 8,$ and 10 at%) powder mixture are checked by SEM. We know that the milling process consists of three main steps: fracturing, steady-state and cold welding [23]. From Fig. 3 ($a_1, b_1, c_1, d_1, e_1,$ and f_1), it is seen that un-milled (0 h milled) powders (iron, nickel, and titanium) contain fine particles with irregular shapes having a varying particle size from 7–80 μm . But after 4 h milling in Fig. 3 ($a_2, b_2, c_2, d_2, e_2,$ and f_2), flattening of powder particle occur by plastic deformation due to the ductile nature of all powders. In this case, particle size increased with irregular shape and produced a mixture with a wide particle size distribution (12–94 μm). But further milling (after 8 h) for Fig. 3 ($a_3, b_3, c_3, d_3, e_3,$ and f_3), powders are strain hardened by heavy plastic deformation during milling and become brittle nature. In this case, no agglomeration and cold welding occur over fracturing mechanisms. So, the particle size is reduced and producing a mixture of semi-spherical with a narrow size distribution (6–58 μm) is developed. Hence a more homogenized mixture was obtained. The contamination (Fe/Cr) during the MA process is common during alloyed powders from the SS vial and ball. The contamination amount depends on the atmosphere, medium, time, and intensity of milling and powder nature hardness/strength [21]. Table 4 shows EDS analysis of different composition powder for 0, 4 and 8 h of milling. According to the analysis, 0 h milled or before milling the element distribution is non-uniform because Ti element is present in a high percentage. Then after 4 h of milling elemental distribution of Ni, Ti, and Fe is not uniform, so the powder particle mixture is not homogenized and also, no other element presents like Cr except 0Fe composition powder (Fe

impurity present). But after 8 h of milling, a homogenized powder mixture was obtained and a small amount of Cr impurity was seen. Also, the present element is relatively close to the composition of the powder.

Figure 4 shows the particle size analysis of milled powder for 10Fe composition powder. Figure 4a shows the cumulative size distribution of powder particles after different hrs of milling. It is seen that milled after 4 h, the curve shift to the right side, indicating particle size increases. But milled after 8 h, curves shift to the left side, which means particle size decreases and the gradual refinement of powders takes place. Figure 4b shows that the $d_{10}, d_{50},$ and d_{90} variation during milling. It observed that milled after 4 h, all values increase and then this value decreases milled after 8 h, showing finer powder takes place. In this case, the total milling process can be divided into two stages are shown in Fig. In between 0 and 4 h (stage I), it is seen that $d_{10}, d_{50},$ and d_{90} values increase (means powder particle size increases) because powders particle is ductile and soft; hence powder flattening initially occurs. This is well in accordance with Fig. 3 ($a_2, b_2, c_2, d_2, e_2,$ and f_2). Between 4 and 8 h (stage II), the d_{10}, d_{50} and d_{90} values drastically decrease (means powder particle size decreases) due to the strain hardening and fracturing of powder particles. In this stage, particles become hard and brittle due to work hardening and finally reduce the powder size by fracturing. This is well in accordance with Fig. 3 ($a_3, b_3, c_3, d_3, e_3,$ and f_3).

The XRD patterns of $\text{Ti}_{50}\text{Ni}_{50-x}\text{Fe}_x$ ($x = 0, 2, 4, 6, 8$ and 10 at%) powder mixture with respect to milling time are shown in Fig. 5a–f. the initial powder mixture (before milling i.e., 0 h) are sharp crystalline peaks of Ni, Ti, and Fe individual powders. After the milling process (i.e., after 4 h milling), the peak sharpness and their

Fig. 3 SEM micrographs of **a**₁ 0 h, **a**₂ 4 h, **a**₃ 8 h milled 0Fe powder, **b**₁ 0 h, **b**₂ 4 h, **b**₃ 8 h milled 2Fe powder, **c**₁ 0 h, **c**₂ 4 h, **c**₃ 8 h milled 4Fe powder, **d**₁ 0 h, **d**₂ 4 h, **d**₃ 8 h milled 6Fe powder, **e**₁ 0 h, **e**₂ 4 h, **e**₃ 8 h milled 8Fe powder and **f**₁ 0 h, **f**₂ 4 h, **f**₃ 8 h milled 10Fe powder

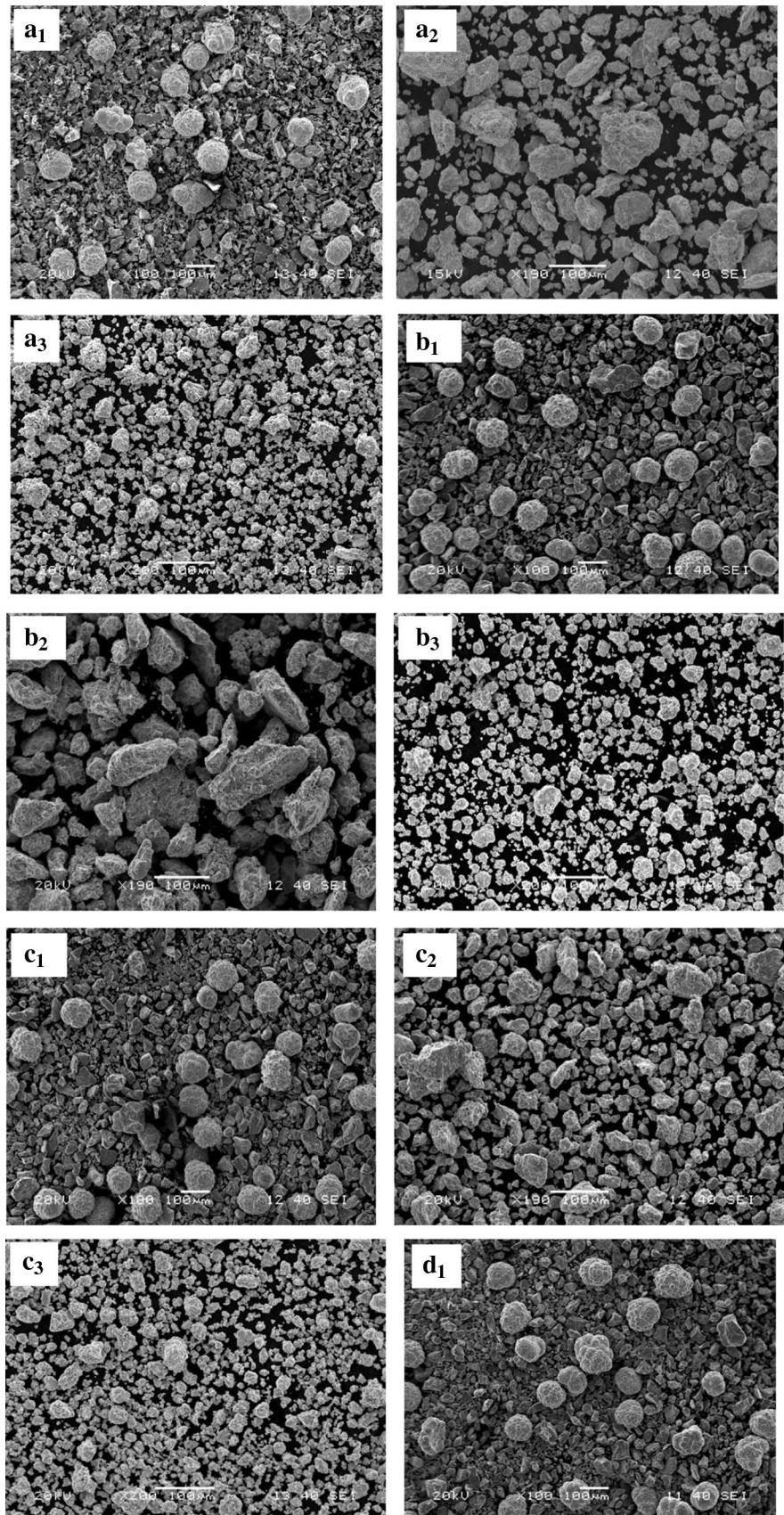
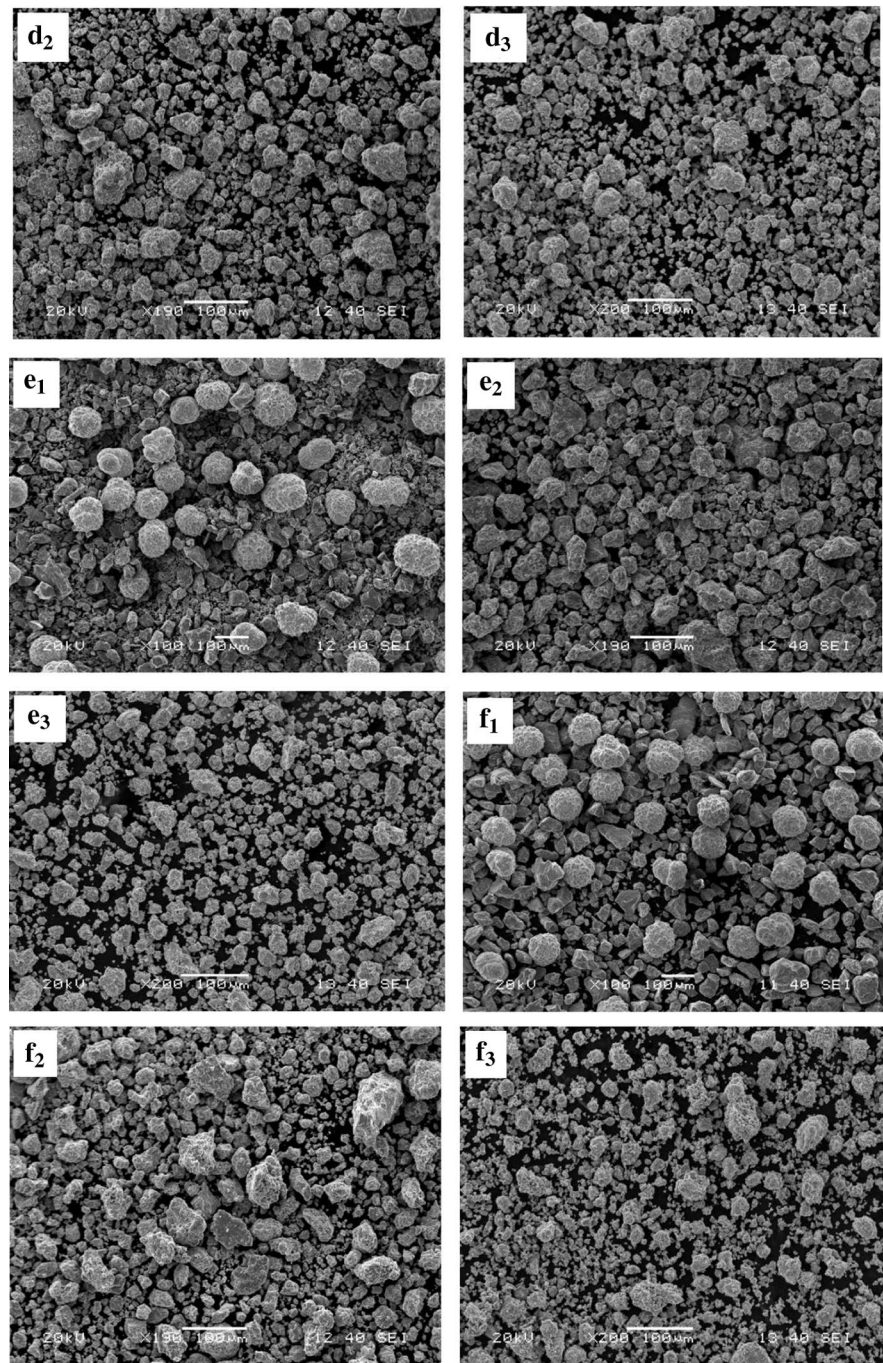


Fig. 3 (continued)

**Table 4** Elemental analysis by EDS of the alloy milled powder 0, 4, and 8 h milling

Samples code	0 h				4 h				8 h			
	Ti at%	Ni at%	Fe at%	Cr at%	Ti at%	Ni at%	Fe at%	Cr at%	Ti at%	Ni at%	Fe at%	Cr at%
0Fe	71.09	28.91	–	–	40.31	58.68	1.01	–	42.95	55.43	1.28	0.34
2Fe	60.43	32.51	7.07	–	44.96	49.98	5.06	–	46.01	50.01	3.50	0.48
4Fe	75.24	17.61	7.15	–	51.73	43.92	4.35	–	44.64	49.57	5.28	0.51
6Fe	66.85	23.06	10.09	–	42.98	45.83	11.20	–	46.21	44.76	8.40	0.63
8Fe	72.16	16.81	11.03	–	51.77	38.89	9.34	–	41.38	47.03	10.82	0.77
10Fe	51.27	31.13	17.61	–	46.56	39.06	14.38	–	40.43	41.96	12.78	0.83

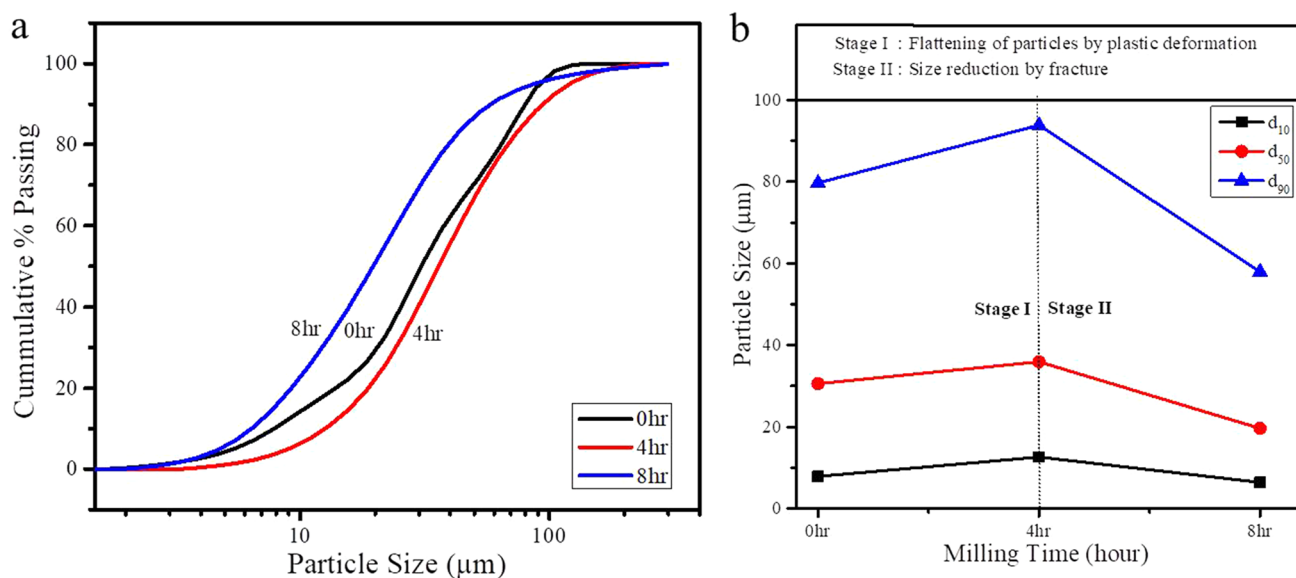


Fig. 4 **a** Cumulative particle size distribution of milled powder particle and **b** variation of d_{10} , d_{50} and d_{90} of milling with milling time for 10Fe powder composition

broadening increase. Also, some peaks of Fe and/or Ti having small intensity are disappeared and some weak peaks are seen by the enlarged XRD image compared to the 0 h milled powder (un-milled powders), and Fe and/or Ti peaks disappear faster than Ni peaks. Also, Ni peaks having small displacement towards lower angles are seen. These results indicate that Ni lattice parameters are increased and few Ti (atomic radius: 0.147 nm) or Fe (atomic radius: 0.126 nm) particles are dissolved into the Ni (atomic radius: 0.125 nm) by solid-state diffusion [26]. But as milling time increases (i.e., after 8 h milling), the peak sharpness of each composition is reduced and their broadening increases due to the high amount of energy and defects produced. With the increase in milling time, some peaks disappeared with respect to the initial powder mixture, this indicates that the alloying process started but was not alloyed because the only elemental peak was present are shown in Fig. 5a–f. And also, Ni peaks are shifted to higher angles due to the presence of traces of impurities of Cr particles from balls and vials dissolving in Ni lattice, and their amounts increase with milling time. The Fe and Cr contamination amount after 8 h milling was reported about less than 1.28 and 0.83 at% respectively by EDS analysis which contracts the lattice and causes peaks to shift to the higher angles [27]. Also, stacking faults is another reason for peaks that shift to higher angles. Heavy cold deformation in Ni produces stacking faults on (111) planes which cause the peak shift to the higher angles [27]. After 8 h milling, new chemical

or intermetallic compounds are not formed during the MA process.

3.2 Porosity and Density of the Green Compact

Figure 2b shows the theoretical density, green density, and green porosity as a function of different % Fe. The decrease in the theoretical density of TiNiFe alloy when the iron content is increased from 0 to 10 at% because the density of iron (7.78 g/cm^3) is lower than nickel (8.90 g/cm^3). Also, it decreases green density with increased iron content because introduced pores during compacting cause that lower green density compared to the theoretical density. The total amount of porosity increases when increasing of Fe amount from 0 to 10 at% because the density of the powder mass decreases. This increases in green porosity for the alloy with values of 27.25%–31.8% due to the introduction of Fe from 0 to 10 at%.

3.3 Sinter Sample Characterization

3.3.1 XRD analysis

Figure 6 shows the XRD patterns of all sintered samples and Table 5 shows present elements and intermetallic in each sample with their reference code. After sintering, several intermetallic phases such as NiTi_2 , Ni_3Ti , Ni_2Ti , Fe_2Ti , and NiTi formed along with elemental Ni, Fe, and $\alpha/\beta\text{-Ti}$. It indicates that the full diffusion or inter-diffusion has been carried out and reactions between powders are not fully taken

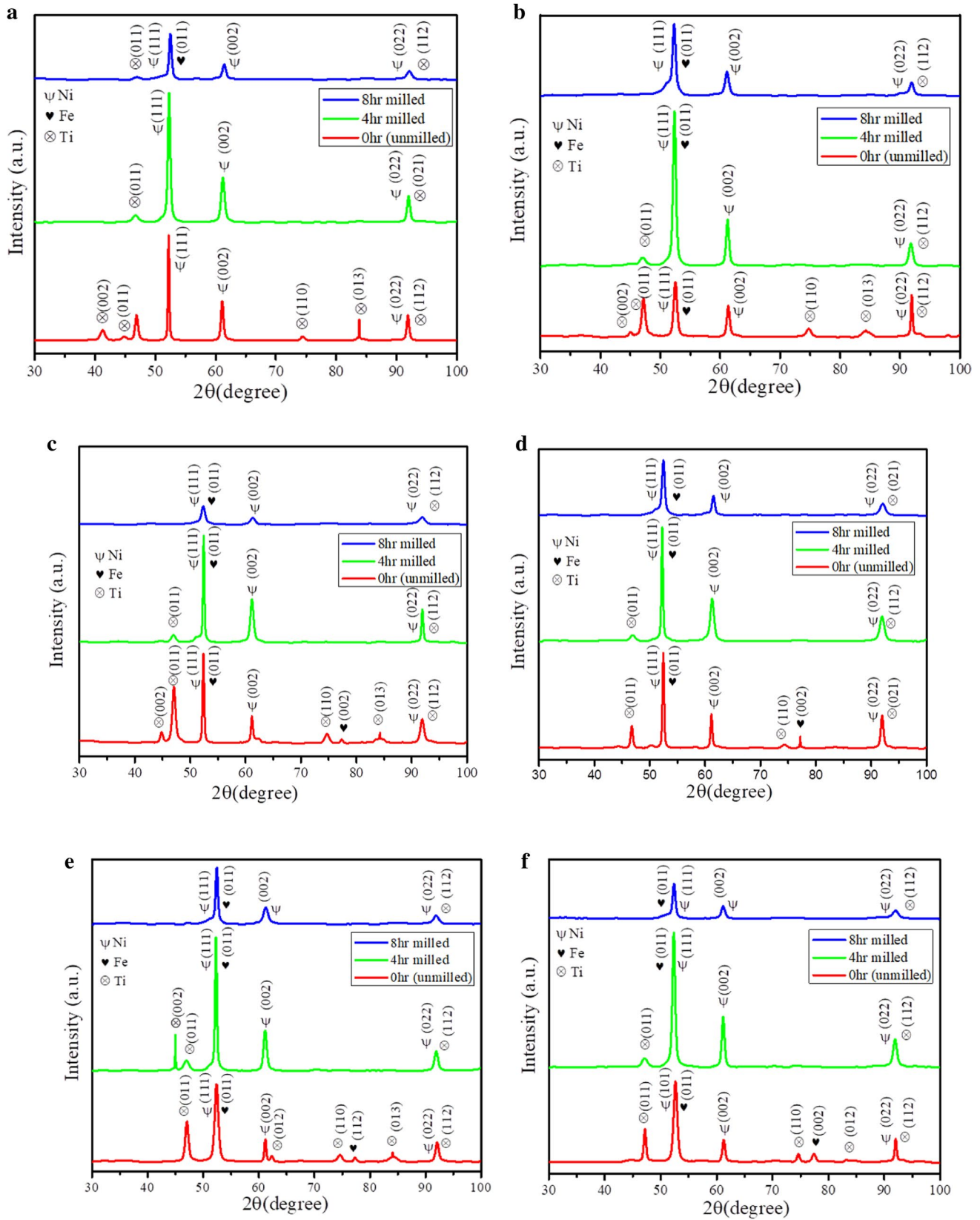


Fig. 5 XRD analysis of milled powder at 0 h, 4 h, and 8 h milling times for **a** 0Fe, **b** 2Fe, **c** 4Fe, **d** 6Fe, **e** 8Fe, and **f** 10Fe samples

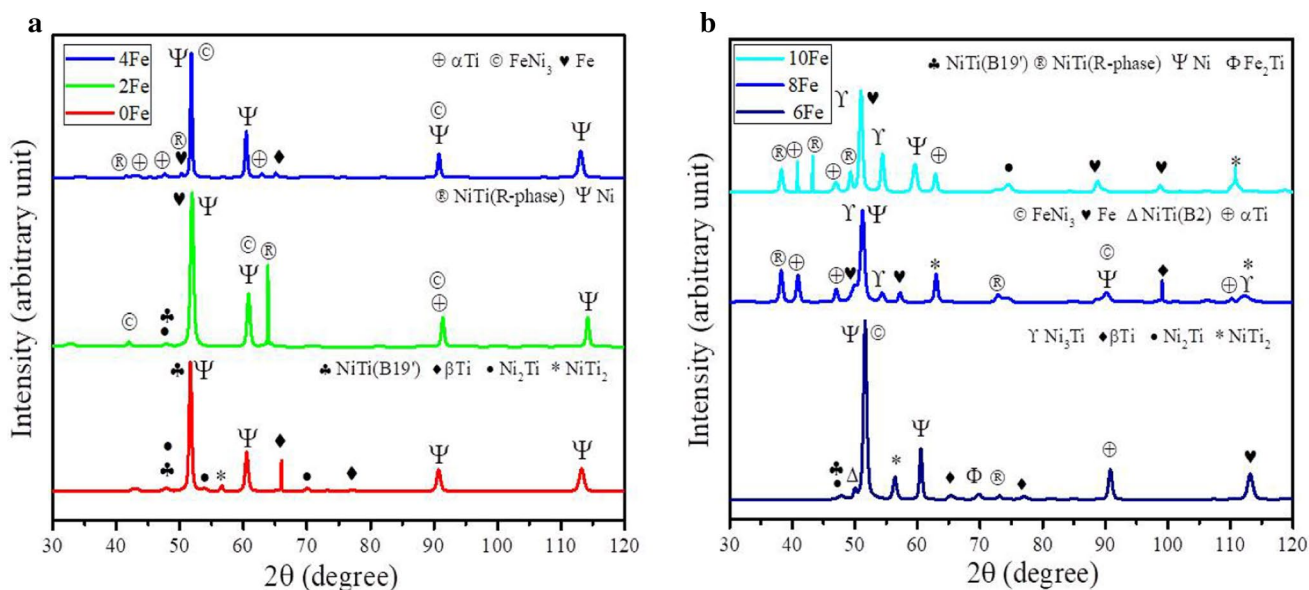


Fig. 6 XRD pattern of a 0Fe, 2Fe, and 4Fe and b 6Fe, 8Fe, and 10Fe sintered samples

Table 5 XRD results of samples

Samples name	Element and compound name	Reference code	Samples name	Element and compound name	Reference code
0Fe	Ni	98-011-5267	2Fe	Ni	98-006-2718 96-901-2983
	β-Ti	98-007-1959		Fe	98-002-1567
	NiTi(B19')	98-008-0888		NiTi(B19')	98-008-3859
	β-Ti	98-002-3322		NiTi (R)	98-010-8909
	Ni	96-901-3006		Ni ₂ Ti	98-007-5005
	NiTi ₂	98-007-5004		FeNi ₃	98-002-3843
4Fe	Ni ₂ Ti	98-007-5005	6Fe	α-Ti	98-009-2049
	Ni	98-011-5267 96-901-3005		Ni	98-011-5267
	NiTi(R)	98-011-3054		Fe	96-901-4606
	FeNi ₃	98-008-8173		β-Ti	98-010-3647 98-002-3322
	Fe	98-008-8005		NiTi(B2)	98-011-4255
	α-Ti	98-008-0571		NiTi (R)	98-010-3230
8Fe	β-Ti	98-010-3647	10Fe	Ni ₂ Ti	98-007-5005
	Ni	98-011-6293		α-Ti	98-006-2696
	α-Ti	98-007-1721		FeNi ₃	98-002-3843
	FeNi ₃	98-007-3211		NiTi ₂	98-000-4100
	Fe	98-008-7998		Fe ₂ Ti	98-008-8363
	β-Ti	98-010-3647		NiTi(B19')	98-008-3859
	NiTi (R)	98-010-8909		Ni	98-011-6293
	Ni ₃ Ti	98-009-2340		α-Ti	98-009-2053
NiTi ₂	98-007-5004	Fe	98-006-2714		
			Ni ₂ Ti	98-007-5005	
			NiTi (R)	98-010-3230	
			Ni ₃ Ti	98-009-2340	
			NiTi ₂	98-007-5004	

place because few elemental peaks still exist after sintering. The different phase formed in the samples also gives evidence in SEM–EDS data. According to B. Liu et al., if the free or unreacted element is the main phase with some intermetallic compound then inadequate sintering will be done [25]. Also, increased temperature helps grow diffusion rates between Ti, Fe, and Ni atoms resulting from unreacted elements to respective intermetallic. For example, the transformation of α -Ti to β -Ti and β -Ti to Ti–Ni intermetallic (i.e., NiTi₃, NiTi and Ti₂Ni) has been observed. The XRD results in Table 6 show that pure Ni, and Fe exist as a major phase for all samples. It indicates that the self-and inter-diffusion of Ni, Fe, and Ti are not enough for this sintering temperature or in other words low diffusion rate of Ni, Fe, and Ti atoms at this temperature. According to phase diagram, the sintering temperature 1050 °C which is higher than 942 °C (lowest temperature liquidus line) in Ni–Ti phase diagram but it lower than lowest temperature liquidus line in Fe–Ti and Fe–Ni phase diagram. Due to this reason Fe, Ni, β -Ti element is present during analysis.

NiTi (as major phase) and NiTi₂ phases are present for the 0Fe sample and Ni₃Ti (as major phase) and NiTi₂ (as secondary phase) for the 8Fe sample. The Ni₃Ti, NiTi₂, and NiTi phase presence can help in improve the properties like hardness and strength of a sample. Figure 6a shows that, in the 0Fe sample the largest peak is at 51.65° which corresponds to NiTi (B19') intermetallic compared to other composition samples. This phase helps for the better strength of the alloy. But compared with the 2Fe and 4Fe samples, the largest change occurs in the pattern because of the presence of iron addition. Due to this, several small peaks like NiTi (B19'), Ni₂Ti, NiTi₂ and β -Ti that disappeared are shown in Fig. 6a. Due to this reason, it decreases the properties of samples like hardness, strength etc. Again, several numbers of small and medium peaks appeared in 8Fe and 10Fe samples are shown in Fig. 6b, which helps for better properties such as hardness and wear resistance. The Fe₂Ti and Fe₃Ni intermetallic peaks present are indicate that all the Fe additions dissolve into the Ni and Ti particles. The amount of Ni₂Ti and NiTi₂ peaks reduces while Fe₂Ti and Fe₃Ni increase. So, Fe has a greater tendency to react with nickel than titanium and forms a large number of compounds with nickel. This is supported by the thermodynamic data.

No Fe-based ternary intermetallic found in XRD analysis because the XRD database does not have any entries like (Fe, Ni)Ti₂ and (Fe, Ni)Ti compounds. Because Fe is a low amount in this composition, so their XRD peaks are related to NiTi and NiTi₂, respectively.

3.3.2 SEM–EDX Analysis

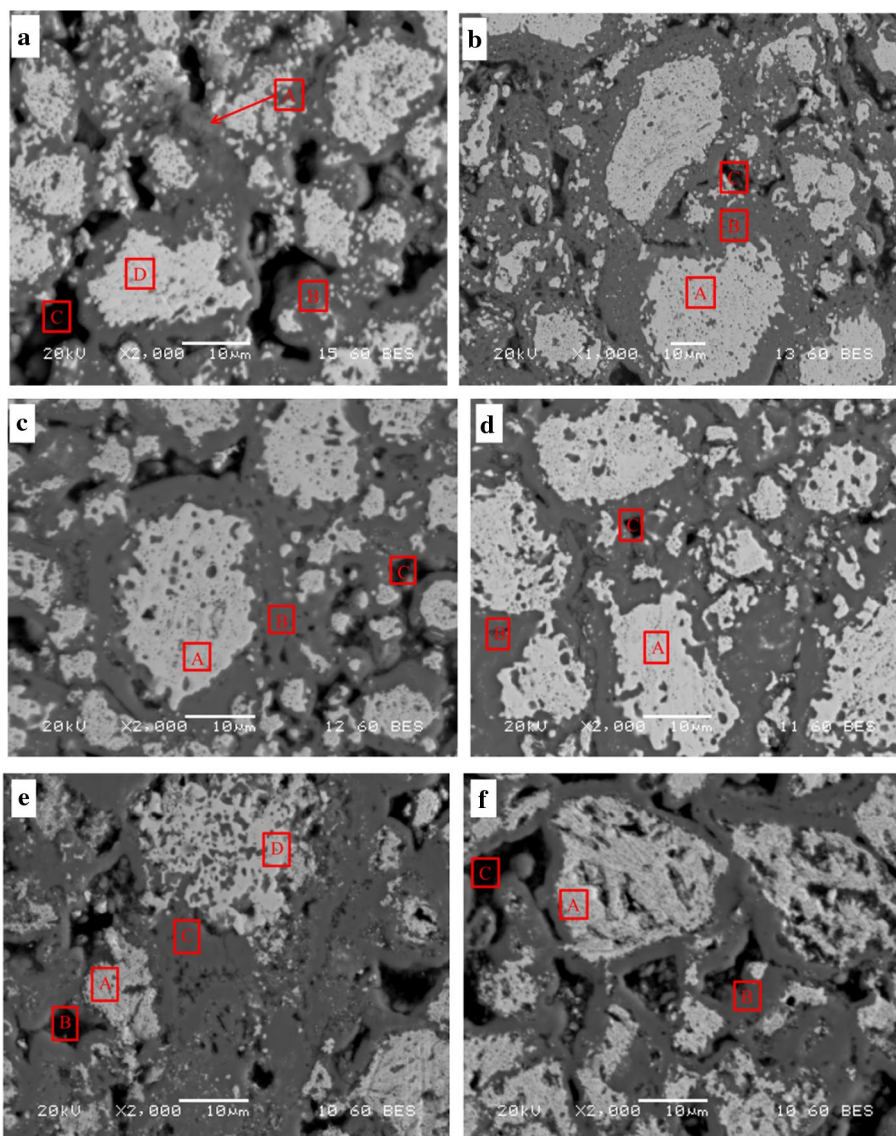
Figure 7a–f and Table 7 show backscattered SEM images with EDS spectra for all sintered samples. It shows that there are 3-different contrasting areas observed in samples, including grey, white and dark phases. The grey and dark areas are Ti-rich-based phases i.e., α -Ti (which is a matrix of the alloy) of more than 98.2 at% Ti and β Ti of less than 94.2 at% Ti phase with a small amount of Fe and Ni. In this region, pure Ti is not present which contains Ti along with Fe and Ni contains more than 1 at%. White phases are (Ni, Fe)-rich phase i.e. undissolved Ni, Ni₂Ti, and Ni₃Ti phase with a small amount of Ti. In this region, pure Ni is not present which contains Ni and Fe along with Ti having more than 5 at%. The phase types are confirmed by both XRD and EDS analyses. The Ni, Fe, Fe₂Ti, FeNi₃, and Ti₂Ni phases are seen in the XRD pattern but not in the SEM image. It is known that the volume fraction of this phase is low. Also seen from the SEM image is that for the 0Fe sample, NiTi phase (small area) present in α -Ti matrix phase but other composition sample for 2Fe to 10Fe is not present. It indicates that only the primary reaction is complete but the secondary reaction not start in the 0Fe sample due to this reason small portion is NiTi phase present in α -Ti matrix phase. But in case of 2Fe to 10Fe sample, partially the primary reaction takes place and a secondary reaction is not started due to this reason is more amount secondary phase present such as α -Ti as a matrix phase and (Ni, Fe)-rich phase. The presence of elemental phases and more amounts of secondary phase (such as Ti-rich phase and (Ni, Fe)-rich phase) indicates that the sintering process is not fully diffusion takes place at this sintering temperature.

Table 7 shows the chemical composition of different region. It is observed that with an increase in Fe at%, there is a reduction in Ni concentration and Ti amount changes in both phases i.e., Ti-rich and (Ni, Fe)-rich phase. Due to the solid solution of Fe that replaces the Ni atom, such way

Table 6 XRD results of different samples with major phase (M), secondary phase(S), and minor phase (m)

Samples name	Ni	α -Ti	β -Ti	NiTi	Ni ₃ Ti	Fe	FeNi ₃	NiTi ₂	Fe ₂ Ti	Ni ₂ Ti
0Fe	M	–	m	M	–	–	–	m	–	m
2Fe	M	m	–	–	–	M	S	–	m	m
4Fe	M	m	m	m	–	m	M	–	–	–
6Fe	M	S	m	–	–	–	M	m	m	m
8Fe	M	m	m	–	M	m	m	S	–	–
10Fe	S	m	–	–	M	M	–	m	–	m

Fig. 7 SEM micrographs of **a** 0Fe, **b** 2Fe, **c** 4Fe, **d** 6Fe, **e** 8Fe, and **f** 10Fe samples



that reduces Ni content, and the Fe content increases in both phases. But the “Ni + Fe” to Ti ratio is unchanged in the TiNiFe alloys. Also, see that the element Ni and Fe are faster diffusion rates in the α -Ti phase are compared to the β -Ti phase than the self-diffusion of Ti because based on literature review. Here, the diffusivity of Ni and Fe are similar in Ti and it increases with increasing temperature [28]. Based on the above mechanism, the hardness value is more in the α -Ti (matrix phase) phase compared to the β -Ti.

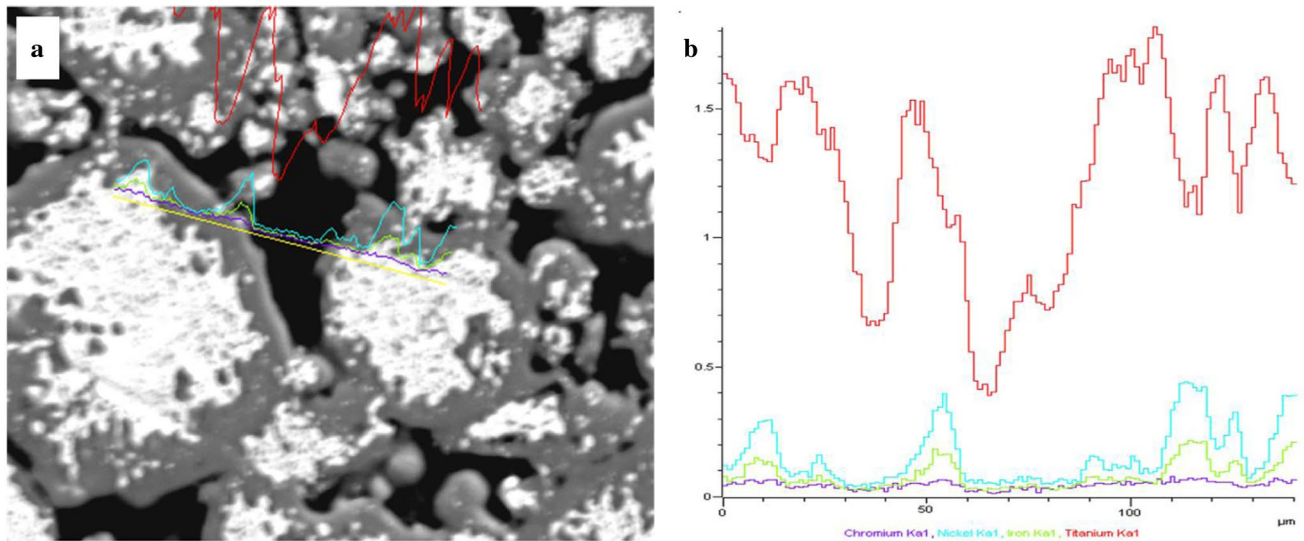
Figure 8a and b show the line-scan analysis of the 2Fe sample. From the figure, it is seen that how element varies from the white phase (one region) to white phase (another region) through the grey and dark phase. The amount of Ti in the dark and grey region is more but other elements are low. The Fe and Ni are high amounts in the white region and Ti is a low amount. Also confirmed a small amount of Cr is present in the sample. The lower Gibbs free energy helps

the intermetallic compounds formed after sintering process. After the process, all-atom diffuses and the formation of intermetallic compounds. But the presence of Cr and Fe (in the case of the 0Fe sample), which the decreases diffusion rate (slow down reaction rate) between Ni, Fe, and Ti. Also, the Cr melting point is higher than Ni, Ti and Fe is the reason for the presence of unreacted elements in the sample. These free elements act as barriers against further reaction. Due to this reason, full diffusion does not take place at this sintering temperature. So, the higher sintering temperature (not less than 1050 °C) is needed for this alloy for better properties.

Figure 9 shows the elemental area mapping of the 4Fe sample which shows the distribution and presence of Ti, Ni, Fe, and Cr elements in the microstructure by means of different colours. It concludes that elements are uniformly distributed throughout the microstructure and the dark and grey

Table 7 Chemical compositions of various regions are marked in Fig. 7

Samples name	Regions in micrograph	Composition (at%)				Phase
		Ni	Ti	Fe	Cr	
0Fe	A	47.87	50.61	1.10	0.42	NiTi
	B	38.41	59.96	1.05	0.58	Ti-rich
	C	10.93	89.77	1.03	0.58	β -Ti
	D	70.82	28.55	1.02	0.61	Ni ₂ Ti
2Fe	A	73.68	19.46	6.23	0.63	(Ni, Fe)-rich
	B	0.89	96.79	1.73	0.59	α -Ti
	C	31.61	66.78	1.11	0.50	Ti-rich
4Fe	A	55.93	19.42	24.33	0.32	(Ni, Fe)-rich
	B	2.12	96.69	0.80	0.39	α -Ti
	C	7.37	88.98	3.18	0.47	β -Ti
6Fe	A	76.09	6.66	16.85	0.52	(Ni, Fe)-rich
	B	2.92	96.26	0.60	0.22	α -Ti
	C	6.89	89.45	3.18	0.48	β -Ti
8Fe	A	57.59	16.60	25.28	0.53	(Ni, Fe)-rich
	B	4.97	91.72	3.00	0.31	β -Ti
	C	0.81	98.56	0.50	0.13	α -Ti
	D	67.29	21.56	10.56	0.59	Ni ₃ Ti
10Fe	A	45.70	21.98	31.94	0.38	Ni ₃ Ti
	B	1.03	97.99	0.82	0.16	Ti
	C	13.17	75.24	11.24	0.36	β -Ti

**Fig. 8** Line scan analysis of elemental Cr, Fe, Ti, and Ni change concentration with respect to a different phase in the 2Fe sample

region belongs to Ti-rich phase and white phase belongs to (Ni, Fe) rich phase; this is also confirmed from Fig. 8 and Table 7. From the figure, it is seen that Ti-rich phase (i.e. α -Ti and β -Ti) in microstructure is more compared to (Ni, Fe) rich phase and the Fe concentration and distribution in the Ni was more than Ti which is also confirmed in EDX analysis shown in Table 7. Also seen that Ni particle consumed more than Ti during diffusion process, so the majority region

of the microstructure of alloy contains higher Ti values i.e. Ti-rich phase and resulted more α -Ti and β -Ti phases in the TiNiFe alloy. When correlating these elemental area mapping with EDS analysis of a sample, results shows that the distribution and presence of individual elements and different intermetallic phases. Also, Cr distributions indicate that the Cr is slightly present in alloy sample.

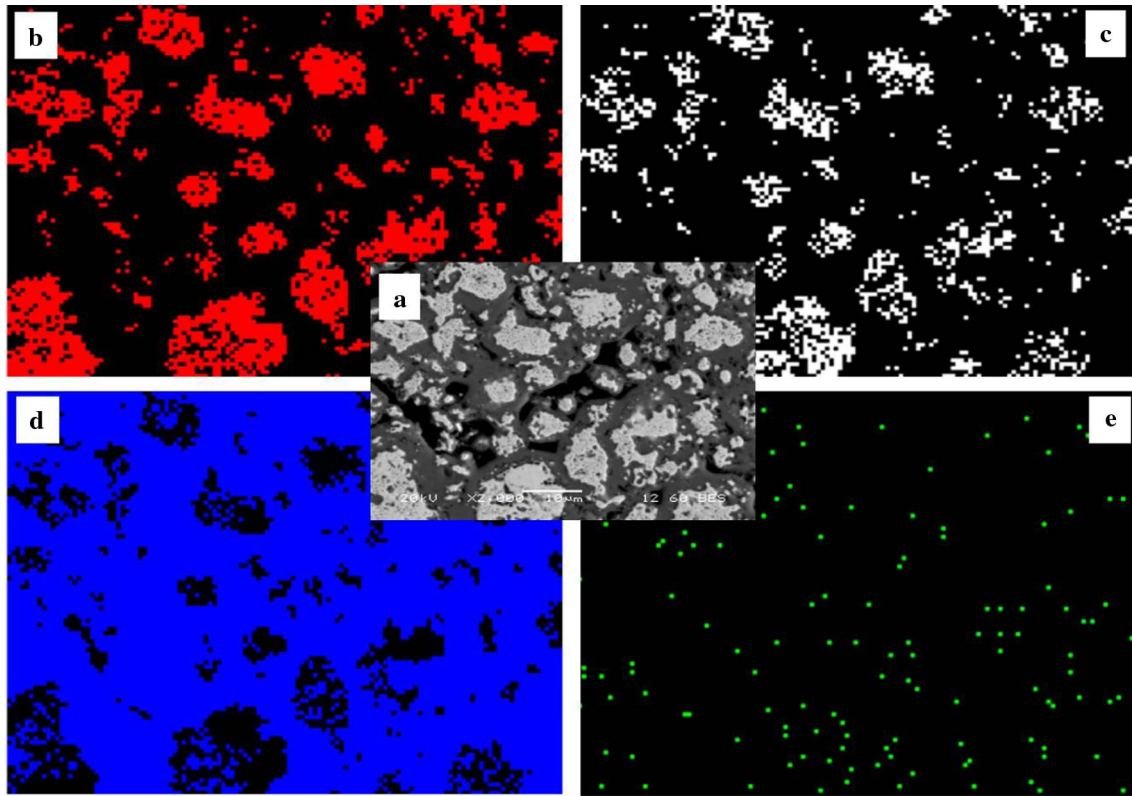


Fig. 9 Elemental mapping of 4Fe sample: **a** Backscattered SEM images, **b** Ni, **c** Fe, **d** Ti and **e** Cr

3.3.3 Relative Density and Hardness

Relative density and hardness analysis of sintered samples are shown in Fig. 10. Figure 10a shows that the experimental and relative density values of 8Fe are higher than other

samples. These values decrease from 0 to 2Fe sample then values increase from 2 to 8Fe sample again values decrease due to presence of more porosity amount because porosity percentage is inversely proportional to relative density or experimental density value. Also, see that the experimental

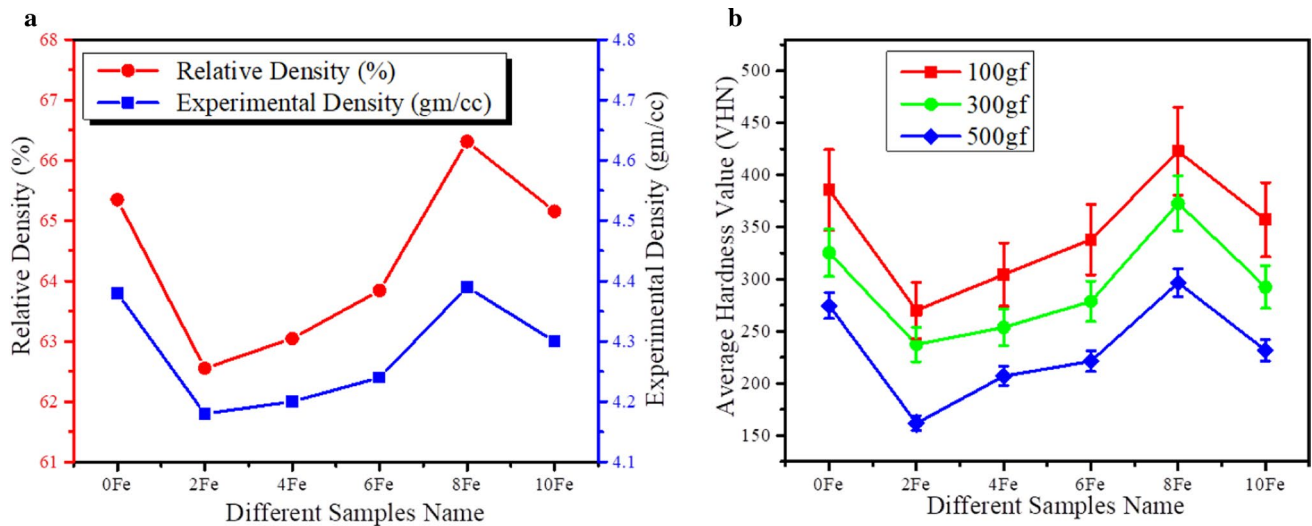


Fig. 10 **a** Experimental and relative density values vs different samples and **b** Hardness values vs different samples

densities are a lower value than theoretical density is due to after sintering the interconnected and isolated pores/voids present and use of purity of raw materials. The Vickers micro-hardness value is calculated using the relation as in Eq. 6 [29].

$$\text{Hardness Value} = 1.8544 \frac{P}{d^2} \tag{6}$$

where P is the load applied in gm-f and d is the indentation diagonal length in μm .

Figure 10b shows the hardness of the sample values measured at 100–500 gf indentation load. It is found that sample hardness values decrease with increased applied indentation load due to the indentation size effect, and it happened due to the strain gradient effect and surface effect [30]. The hardness of the tested specimen is a measure of the indentation depth, which is inversely proportional to hardness based on Eq. 6 [31]. Therefore, with the applied load increase from 100 to 500 gf, the increased indentation depth and so decreases the hardness values are shown in the figure. Also seen from the figure, increasing the load amount decreases the values of variation of hardness values. Again, hardness value increases due to density value increases because of the less number of voids or lower porosity values. This value increase may be due to the support force increase of the pore walls [32], bonding strength and hinders grain growth. 8Fe alloy sample is higher values than other samples may be due to amount of hard phase increases or some new phase formed i.e., presence of Ni_3Ti and NiTi_2 phases or due to the change of microstructure morphology induced by iron addition. According to literature Ye et al. [33], Ni_3Ti + NiTi_2 are present in the sample as a major phase then its hardness values higher. The Ni_3Ti (major phase) and NiTi_2 (secondary phase) phases are present in the 8Fe sample shown in Table 6. So based on this 8Fe are higher hardness compared to other sample. The porosity decreases result because the support force of pore walls decreases, which naturally increases the samples hardness [32].

Table 8 gives the values of the relative densities without and with the pores considered and the porosity percentage that is calculated from Eqs. 7–9. It shows that the lower sample relative density is obtained when both external and

internal pores are considered. If only external pores are considered, then relative density values will be in the range of 62%–67%. It concludes that 8Fe samples show the minimum porosity and maximum relative density compared to other samples. The obtained results indicated that the density increases and porosity decrease with the increase of Fe percentage from 2 to 10Fe sample. The reason for alteration of porosity values is due to after sintering, necks are created between powder particles, and then necks combine together causing density increase and porosity decrease [34].

In Archimedes principle, there are two formulas for density calculation [35–37].

Formula 1 : Density of sample
(only external pores considered) = $\frac{m_1}{m_1 - m_2} \times \rho_w$ (7)

Formula 2 : Density of sample
(both internal and external pores considered)
= $\frac{m_1}{m_3 - m_2} \times \rho_w$ (8)

Porosity (%) = $\frac{m_3 - m_1}{m_3 - m_2} \times 100$ (9)

where m_1 = mass of sample taken in air, m_2 = mass of sample when submerged in water, m_3 = soaked mass of the sample, and ρ_w = density of water.

3.3.4 Compressive Strength

Figure 11a shows the true stress–true strain and Fig. 11b shows variation of yield strength, compressive strength, and elastic modulus values of different alloy samples. Here, the compressive process is classified into three areas: (a) a linear elastic deformation region, where the sample elastic modulus is considering the slope; (b) a plastic yield deformation region, where the sample compressive strength is considered to appear peak stress; and (c) a rupture and densification region, where the pores walls are collapse and the occur sample rupture [38]. Figure 11a

Table 8 Relative densities without and with the pores consider and porosity percentage

Sample name	Rel. density (only external pores) (%)	Rel. density (both external and internal pores) (%)	Porosity (%)
0Fe	65.40	53.65	17.96
2Fe	62.48	47.53	23.93
4Fe	62.98	49.15	21.95
6Fe	63.83	50.63	20.68
8Fe	66.31	54.76	17.31
10Fe	65.18	52.73	19.1

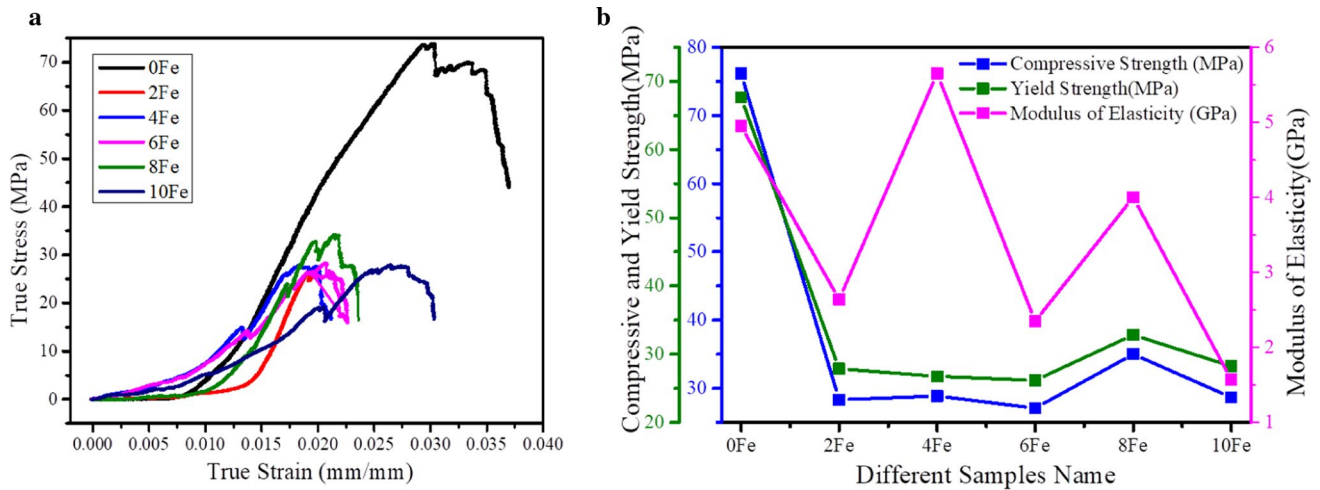


Fig. 11 **a** True stress–true strain curve and **b** Yield strength, compressive strength, and elastic modulus values of different samples

shows significant fluctuation at end of the curve because: (1) brittle nature of alloy sample and (2) during the compressive loading, contact between the particles are broken, so the reduced strength. Again, the other particles instantly carry that load up to their point of breaking, so the increased strength again. In this way, all particles have to carried the load up to their point of breaking. From this figure, it concludes that true stress, yield, and compressive strength decreased with the increasing porosity of the TiNiFe alloy. The sample yield and compressive strength with a porosity of 17.31% are 32.83 MPa and 35.01 MPa respectively. By increasing the porosities, they decreased to 27.87 MPa and 28.32 MPa respectively with a porosity of 23.93% are shown in Table 8. The load-bearing area of the sample decreases with porosity increased due to pores increases, which helps to decrease compressive strength and compressive strain [39].

But if compared with hardness values, it found that sample yield and compressive strength increases with hardness increases from 2 to 10Fe sample except for 6Fe sample. 6Fe sample show a reduction in yield and compressive strength because of more brittle nature and so, the sample unable to carry the load but 0Fe sample are a high yield and compressive strength value due to the presence of martensites phase which helps capable of carrying maximum load compared to other. The presence of martensites (B19') phase in a sample provides a result in the rapid stress increase with deformation increased [38]. Also, during loading in the compression test, this phase provides the load-carrying capacity, and hence, the strength is improved. Sample without iron content (0Fe) has higher true stress values (i.e., yield and compressive strength values) than other composition samples because of the presence of NiTi (B19') phase are shown in Fig. 7a. From this figure, it concludes that iron

addition to binary NiTi alloy does not improve mechanical properties i.e., yield and compressive strength in this sintering temperature.

3.3.5 Wear Resistance

In the unlubricated wear test, the wear resistances are depending on the wear amount and the friction coefficient [40]. For example, the higher strength samples facilitate a small contact area and a weak adhesion between mating surfaces, causing a low friction coefficient and small wear amount [41]. The wear performances are affected by some factors such as the hardness, porosity, strength, temperature, and toughness of the alloy sample. Equations 10 and 11 are used to determine sliding distance [42] and friction coefficient respectively [43, 44]; in the sliding wear analysis;

$$\text{Sliding Distance} = \frac{R}{60} * t * 2\pi r \quad (10)$$

$$\text{Friction coefficient}(\mu) = \frac{F}{N} = \frac{A * S}{N} \quad (11)$$

where R is rpm by the ball on a sample surface, t is the time in a sec, r is the track radius in mm, F is the frictional force, S is shearing stress, A is apparent contact area and N is the normal load applied.

Figure 12 shows the wear depth and friction coefficient variation with respect to sliding distance using Si₃N₄ ball on the surface. It is seen that each sample shows different wear behavior due to different average friction coefficient values. Also, the friction coefficient variation in the Fig. 12a with increasing sliding distance shows the wear

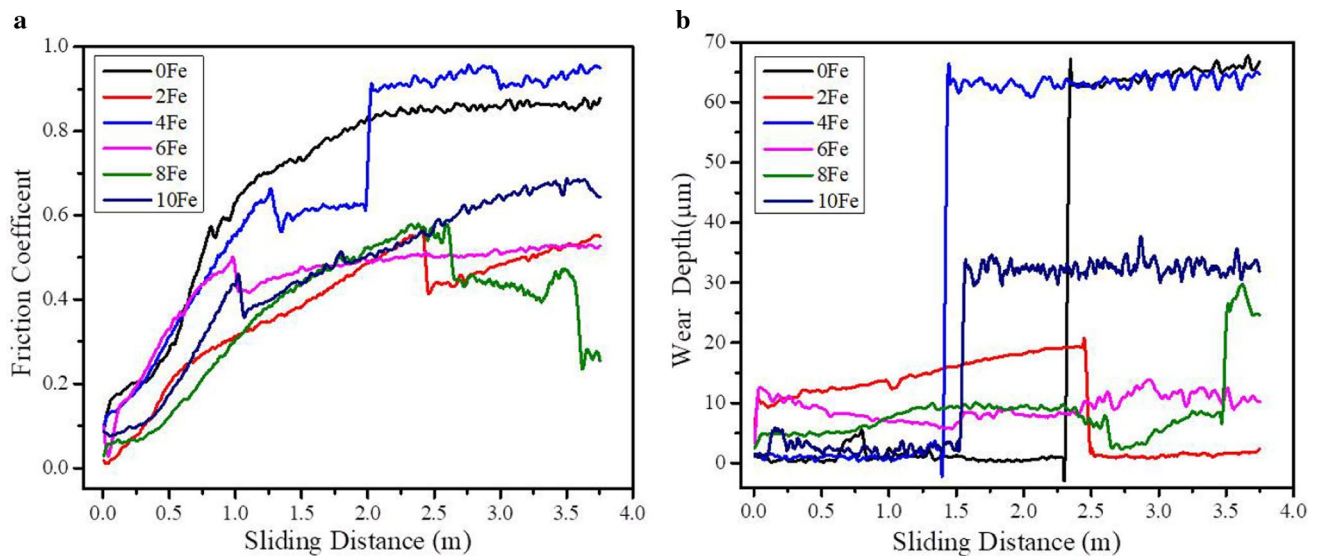


Fig. 12 **a** Friction coefficient and **b** Wear depth vs sliding distance of different samples

debris removed. The average friction coefficient value of 0.37 for 8Fe is lower than other samples due to higher hardness and also the presence of fine Ni_3Ti precipitates in the microstructure [42]. Based on Archard's theory, hardness is related to wear so wear resistance values are the same as their hardness values. After the wear behavior study based on the friction coefficient vs sliding distance plot, wear depth increases along with sliding distance are shown in the Fig. 12b. Also wear depth indicates wear resistance because both are inversely proportional to each other. Therefore, the lower wear depth, the higher wear resistance, and vice versa. It is seen in Fig. 12. The 0Fe sample is a higher wear depth and the average friction coefficient values compared to other samples and among other the 8Fe sample are the lower average friction coefficient values and wear depth. So 8Fe samples are higher wear resistance than other sample. The 2Fe sample shows a low friction coefficient value is 0.38 after 8Fe sample due to higher porosity value (23.93%) and this also similarly happens for the 6Fe sample (i.e. friction coefficient value of 0.44 and porosity value of 20.68%). Based on literature, the higher porosity sample shows lower friction coefficient value (i.e. better wear resistance) than rest of samples [45]. During the friction process, higher wear resistance (low wear removal) depends on the ability of high elastic deformation (i.e., low plastic deformation) between the friction pair [40, 46].

From the worn surface SEM image are shown in Fig. 13a–f, it was observed that all alloys show a similar type wear track indicating a similar type wear mechanism involved with each sample. From wear track analysis, some scratches, wear debris from the surface are removed to near outside wear surface and few are detached on the surface

because of repeated motion of ball during wear testing. From it concludes that it is under an abrasive wear mechanism [44]. In all cases, the primary wear mechanism is the abrasive type wear because of the difference in the hardness values between the Si_3N_4 ball and the TiNiFe alloy samples [22]. Also, for each composition sample, three-track widths with the different areas are taken and the average value is reported in Fig. 13. 0Fe sample shows higher damage of worn surface compared to other samples which indicate resist of surface ability with respect to sliding wear decreases. From the figure, it is seen that, 2Fe, 6Fe, 8Fe, and 10Fe sample surfaces are slightly worn and the shallow wear depth. So, these samples are higher wear resistance compared to other compositions (i.e. 0Fe and 4Fe) but among them, the 8Fe sample is better to wear resistance compared to all samples. Also from Fig. 13, it found that more track width obtained for sample having more friction coefficient value such as 4Fe, 6Fe and 10Fe sample having friction coefficient value 0.68, 0.44 and 0.46 with wear track width 392.7, 375.7 and 384.8 μm respectively. Therefore, it concludes that higher friction coefficient value of sample having more apparent contact area which satisfies Eq. 11 (i.e. friction coefficient value is directly proportional to apparent contact area) [45]. The wear track width values are well in accordance with friction coefficient versus sliding distances i.e. Figure 12a and wear depth versus sliding distance i.e. Fig. 12b. A small Si peak is seen in the EDS analysis in the wear track region; it comes from a Si_3N_4 ceramic ball due to continual sliding motion on the sample surface. Also, oxygen is seen on the surface due to the Ti is a high chemical affinity with oxygen than other present elements. The oxygen present is more in wear track region (i.e. more oxidation) than outside wear track region (i.e.

Fig. 13 SEM micrographs of worn-out surface **a** 0Fe, **b** 2Fe, **c** 4Fe, **d** 6Fe, **e** 8Fe, and **(f)** 10Fe samples

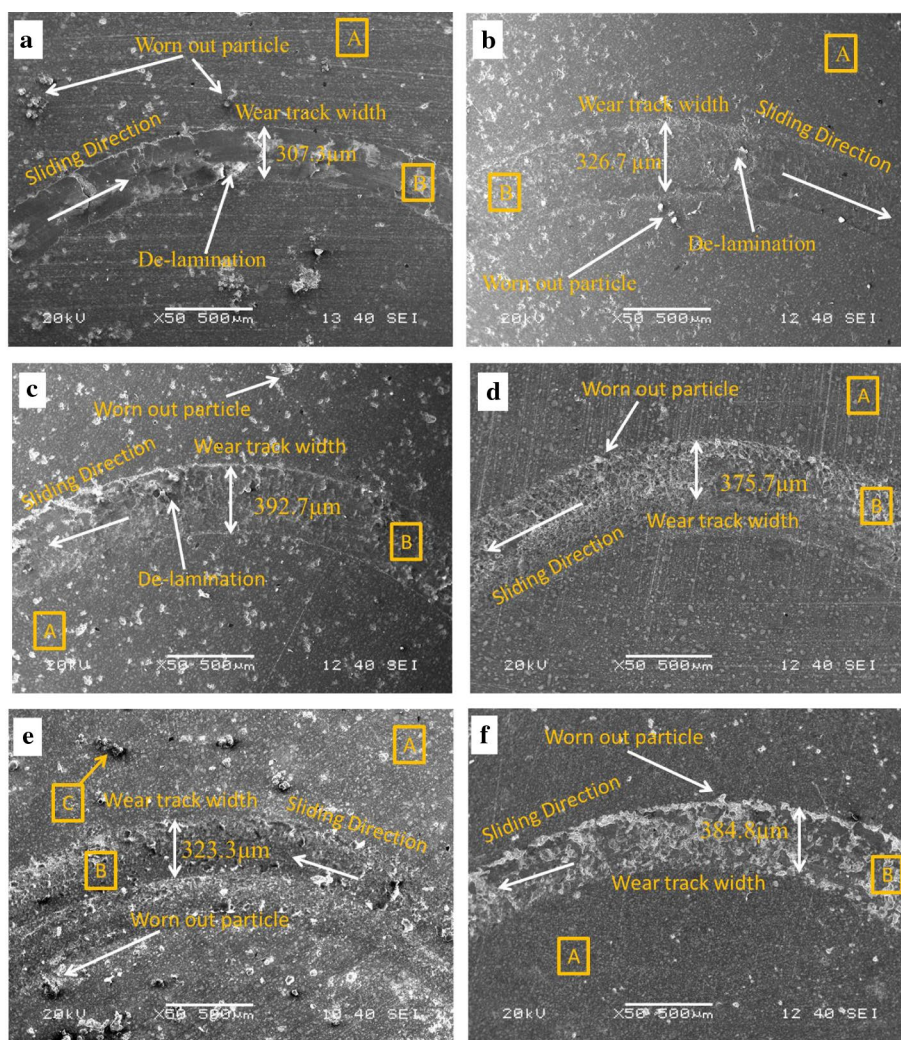


Table 9 Chemical compositions of wear track (B), outside wear track (A) regions and wear debris (C) are marked in Fig. 13

Sample name	Phase region	Composition (at%)					
		Ni K	Ti K	Fe K	Cr K	O K	Si K
0Fe	A	29.60	32.37	1.33	0.31	36.39	–
	B	28.97	25.57	1.08	0.35	43.02	1.01
2Fe	A	16.88	36.99	2.91	0.31	42.91	–
	B	17.64	31.13	2.70	0.32	47.05	1.16
4Fe	A	24.11	32.16	2.89	0.44	40.40	–
	B	22.25	25.57	3.65	0.30	47.22	1.01
6Fe	A	24.45	30.09	5.21	0.42	37.60	–
	B	27.76	28.91	5.42	0.41	37.30	1.20
8Fe	A	29.28	23.34	4.14	0.38	42.86	–
	B	27.15	19.49	4.13	0.39	47.43	1.41
	C	24.10	36.86	7.04	0.17	30.80	1.02
10Fe	A	28.14	23.23	4.53	0.36	43.74	–
	B	28.79	21.33	5.37	0.39	43.36	1.21

less oxidation). The EDS result of wear debris for the 8Fe sample is shown in Fig. 13e and Table 9 which represented by letter ‘C’, it indicating that wear debris composed of oxygen, Ni, Ti, Cr and Fe elements. Therefore, oxidation occurs in wear debris of sample.

3.3.6 Shape Memory Effect

The Shape Memory Effect was calculated by the following equation [23]:

$$\text{Shape Memory Effect} = \frac{d_1 - d_2}{d_1} * 100 \quad (12)$$

where d_1 and d_2 is average indentation diameter of sample in before and after heating in μm .

From Table 10, it concludes that 0Fe, 2Fe and 6Fe samples show better recovery properties than 4Fe, 8Fe and 10Fe samples because due to the presence of martensite NiTi (B19') phase in 0Fe, 2Fe and 6Fe samples which show shape memory effect but secondary phase like FeNi₃ and Ni₂Ti etc. present in 4Fe, 8Fe and 10Fe samples which do not show shape memory effect are shown in Fig. 6. Therefore, the 0Fe and 8Fe samples show highest and lowest SME of 3.74% and 1.11% respectively.

The density, porosity, average hardness, compressive strength, and average friction coefficient values of different samples are represented in Table 11. Table 11 shows the comparison value of physical, mechanical, and wear properties of different alloys. From the table, it concludes that 8Fe alloy

Table 10 SME properties for all composition samples

Sample name	d_1 (μm)	d_2 (μm)	SME (%)
0Fe	153.19	147.46	3.74
2Fe	198.34	191.73	3.33
4Fe	196.535	192.775	1.91
6Fe	162.29	156.595	3.51
8Fe	172.14	170.255	1.10
10Fe	201.12	197.78	1.66

Table 11 Comparisons of experimental and relative densities, porosity, avg. vickers micro-hardness, compressive strength, and Avg. friction coefficient values of different samples in tabular form

Sample name	Experimental density (gm/cc)	Relative densities (%)	Porosity (%)	Avg. Vickers micro-hardness (HV)	Compressive strength (MPa)	Avg. Friction coefficient
0Fe	4.38	65.34	17.96	325.3 ± 22.8	76.16	0.69
2Fe	4.18	62.55	23.93	237.5 ± 16.6	28.32	0.38
4Fe	4.2	63.05	21.95	253.9 ± 17.8	28.88	0.68
6Fe	4.24	63.84	20.68	278.9 ± 19.5	27.09	0.44
8Fe	4.39	66.31	17.31	372.7 ± 26.1	35.01	0.37
10Fe	4.3	65.15	19.1	292.6 ± 20.5	28.67	0.46

sample are higher hardness, density, wear resistance and lower porosity compared to other alloys but 0Fe sample are higher strength compared to the rest composition alloy samples.

4 Conclusions

Effect of Fe in TiNiFe ternary alloy that processed by powder metallurgy has been summarized below:

- From the SEM image and XRD analysis, it concludes that after milling only Ni, Ti, and Fe element are present in milled powder and sintered sample consisting of the (Ni, Fe)-rich and Ti-rich phases is formed such as Ni₃Ti, Ni₂Ti, FeNi₃, Fe₂Ti, NiTi₂, and α/β -Ti with some pores.
- 8 at%Fe sample is higher hardness, lower porosity, higher relative density, and lower friction coefficient of 372.7 HV, 17.31%, 66.31%, and 0.37 respectively than other samples but 0 at%Fe sample are higher SME, yield and compressive strength value i.e., 3.74%, 67.66 and 76.16 MPa respectively. So, different properties are improved by addition of iron as an alloying element in TiNiFe alloy. The best atomic percentage value to be added for this element is (8 at%), which may give maximum hardness up to 372.7 HV.
- 0 at% Fe (without iron) sample are higher SME, yield and compressive strength value because presence of martensites NiTi(B19') phase produce during sintering process which is responsible for the improvement of sample strength and SME.
- Higher wear resistance or the lower friction coefficient value of 8 at%Fe sample compared to other sample because of the presence of Ni₃Ti + NiTi₂ phase or higher hardness value in the sample. The SEM analysis of the worn surfaces shows that the same wear mechanisms of all the samples i.e., abrasive wear mechanism.
- The sintering temperature used in this study is not enough to achieve better properties. The minimum temperature for TiNiFe alloy must be 1050 °C or more. And also, to elimi-

nate undissolved free Ni, Fe element, and α Ti phase, further heat treatment or higher sintering temperature is required.

Acknowledgements This is a part of academic research work and is under the support of Department of Metallurgical and Materials Engineering, National Institute of Technology, Rourkela, India.

Declarations

Conflict of interest There is no funding associated with this manuscript and there are no Conflicts of interests associated with this manuscript.

References

- H. Yin, Q. Sun, J. Mater. Eng. Perform. **21**, 2505 (2012). <https://doi.org/10.1007/s11665-012-0395-9>
- D. Vojtěch, M. Voděrová, J. Fojt, P. Novák, T. Kubásek, Appl. Surf. Sci. **257**, 1573 (2010). <https://doi.org/10.1016/j.apsusc.2010.08.097>
- X. Yin, X. Mi, Y. Li, B. Gao, J. Mater. Eng. Perform. **21**, 2684 (2012). <https://doi.org/10.1007/s11665-012-0376-z>
- L. Stirling, C.-H. Yu, J. Miller, E. Hawkes, R. Wood, E. Goldfield, R. Nagpal, J. Mater. Eng. Perform. **20**, 658 (2011). <https://doi.org/10.1007/s11665-011-9858-7>
- J. Van Humbeeck, Mater. Sci. Eng. A **273–275**, 134 (1999). [https://doi.org/10.1016/S0921-5093\(99\)00293-2](https://doi.org/10.1016/S0921-5093(99)00293-2)
- L. McDonald Schetky, Mater. Design **12**, 29 (1991). [https://doi.org/10.1016/0261-3069\(91\)90089-M](https://doi.org/10.1016/0261-3069(91)90089-M)
- W. Gasior, A. Debski, Arch. Metall. Mater. **57**, 1095 (2012). <https://doi.org/10.2478/v10172-012-0122-4>
- G. Cacciamani, J. De Keyzer, R. Ferro, U.E. Klotz, J. Lacaze, P. Wollants, Intermetallics **14**, 1312 (2006). <https://doi.org/10.1016/j.intermet.2005.11.028>
- H. Xu, C. Jiang, S. Gong, G. Feng, Mater. Sci. Eng. A **281**, 234 (2000). [https://doi.org/10.1016/S0921-5093\(99\)00722-4](https://doi.org/10.1016/S0921-5093(99)00722-4)
- T.-H. Nam, J.-H. Kim, M.-S. Choi, Y.-W. Kim, H.-J. Im, J.-S. Ahn, T. Mitani, J. Mater. Sci. Lett. **21**, 685 (2002). <https://doi.org/10.1023/A:1015720602368>
- L. Heller, P. Šittner, P. Sedláč, H. Seiner, O. Tyc, L. Kadeřávek, P. Sedmák, M. Vronka, Int. J. Plasticity **116**, 232 (2019). <https://doi.org/10.1016/j.ijplas.2019.01.007>
- Shape Memory Alloy Research Team (Smart). <http://smart.tamu.edu> (2001)
- R. Basu, L. Jain, B. Maji, M. Krishnan, J. Alloy. Compd. **639**, 94 (2015). <https://doi.org/10.1016/j.jallcom.2015.03.085>
- A.S. Ferreira, P.R. Rovani, J.C. de Lima, A.S. Pereira, J. Appl. Phys. **117**, 075901 (2015). <https://doi.org/10.1063/1.4907386>
- H.-G. Kim, J. Korean Phys. Soc. **60**, 472 (2012). <https://doi.org/10.3938/jkps.60.472>
- T. Bertilsson, Intermetallic Compound Formation in Ni–Ti–Fe Powder Mixtures, Master's Thesis, Lund University (2018)
- T. Goryczka, J. Van Humbeeck, J. Alloy. Compd. **456**, 194 (2008). <https://doi.org/10.1016/j.jallcom.2007.02.094>
- P. Clayton, Wear **162–164**, 202 (1993). [https://doi.org/10.1016/0043-1648\(93\)90502-D](https://doi.org/10.1016/0043-1648(93)90502-D)
- J. Singh, A.T. Alpas, Wear **181–183**, 302 (1995). [https://doi.org/10.1016/0043-1648\(95\)90037-3](https://doi.org/10.1016/0043-1648(95)90037-3)
- C. Zhang, Z.N. Farhat, Wear **267**, 394 (2009). <https://doi.org/10.1016/j.wear.2008.12.093>
- F. Neves, F.M.B. Fernandes, I. Martins, J.B. Correia, J. Alloy. Compd. **509**, S271 (2011). <https://doi.org/10.1016/j.jallcom.2010.11.036>
- F. Alijani, R. Amini, M. Ghaffari, M. Alizadeh, A.K. Okyay, Mater. Design **55**, 373 (2014). <https://doi.org/10.1016/j.matdes.2013.09.009>
- T.-S. Huang, S.-F. Ou, C.-H. Kuo, C.-H. Yang, Metals **10**, 527 (2020). <https://doi.org/10.3390/met10040527>
- J.L. Xu, X.F. Jin, J.M. Luo, Z.C. Zhong, Mater. Lett. **124**, 110 (2014). <https://doi.org/10.1016/j.matlet.2014.03.088>
- F. Zhang, L. Zheng, Y. Wang, H. Zhang, Intermetallics **112**, 106548 (2019). <https://doi.org/10.1016/j.intermet.2019.106548>
- A.A. Atiyah, A.-R.K.A. Ali, N.M. Dawood, Arab. J. Sci. Eng. **40**, 901 (2015). <https://doi.org/10.1007/s13369-014-1538-0>
- B. Liu, Z. Liu, X. Liu, W. Wang, L. Wang, J. Alloy. Compd. **578**, 373 (2013). <https://doi.org/10.1016/j.jallcom.2013.05.164>
- J.S. Benjamin, T.E. Volin, Metall. Trans. **5**, 1929 (1974). <https://doi.org/10.1007/BF02644161>
- C. Suryanarayana, Prog. Mater. Sci. **46**, 1 (2001). [https://doi.org/10.1016/S0079-6425\(99\)00010-9](https://doi.org/10.1016/S0079-6425(99)00010-9)
- H. Nakajima, M. Koiwa, ISIJ Int. **31**, 757 (1991). <https://doi.org/10.2355/isijinternational.31.757>
- A. Rostami, G.A. Bagheri, S.K. Sadrnezhad, Physica B **552**, 214 (2019). <https://doi.org/10.1016/j.physb.2018.10.015>
- ASTM E384-99, Standard Test Method for Microindentation Hardness of Materials (ASTM International, West Conshohocken, 1999)
- I. Manika, J. Maniks, Acta Mater. **54**, 2049 (2006). <https://doi.org/10.1016/j.actamat.2005.12.031>
- G.M. Pharr, E.G. Herbert, Y. Gao, Annu. Rev. Mater. Res. **40**, 271 (2010). <https://doi.org/10.1146/annurev-matsci-070909-104456>
- J.L. Xu, L.Z. Bao, A.H. Liu, X.J. Jin, Y.X. Tong, J.M. Luo, Z.C. Zhong, Y.F. Zheng, Mater. Sci. Eng. C **46**, 387 (2015). <https://doi.org/10.1016/j.msec.2014.10.053>
- L.L. Ye, Z.G. Liu, K. Raviprasad, M.X. Quan, M. Umamoto, Z.Q. Hu, Mater. Sci. Eng. A **241**, 290 (1998). [https://doi.org/10.1016/S0921-5093\(97\)00505-4](https://doi.org/10.1016/S0921-5093(97)00505-4)
- W. Bolton, *Engineering Materials Technology*, 2nd edn. (Butterworth Heinemann, Oxford, 1988), pp. 50–75
- P.G. Hewitt, J. Suchocki, L.A. Hewitt, *Practice Book: Conceptual Physical Science*, 1st edn. (Benjamin-Cummings Publishing Company, San Francisco, 2003), pp. 37–55
- <https://andersonmaterials.com/density-and-porosity-measurements-of-solid-materials>. Accessed 28 Jan 2020
- Z. Gao, Q. Li, F. He, Y. Huang, Y. Wan, Mater. Design **42**, 13 (2012). <https://doi.org/10.1016/j.matdes.2012.05.041>
- Y.-H. Li, L.-J. Rong, Y.-Y. Li, J. Alloy. Compd. **345**, 271 (2002). [https://doi.org/10.1016/S0925-8388\(02\)00412-7](https://doi.org/10.1016/S0925-8388(02)00412-7)
- R. Yang, W. Ma, C. Duan, Z. Yang, X. Zhang, T. Wang, Q. Wang, Tribol. Int. **140**, 105816 (2019). <https://doi.org/10.1016/j.triboint.2019.06.009>
- V. Mortazavi, M.M. Khonsari, J. Tribol. **138**, 041604 (2016). <https://doi.org/10.1115/1.4032843>
- P. La, Q. Xue, W. Liu, Wear **249**, 93 (2001). [https://doi.org/10.1016/S0043-1648\(01\)00523-3](https://doi.org/10.1016/S0043-1648(01)00523-3)
- S. Wu, X. Liu, K.W.K. Yeung, Z.S. Xu, C.Y. Chung, P.K. Chu, J. Mater. Eng. Perform. **21**, 2622 (2012). <https://doi.org/10.1007/s11665-012-0392-z>
- Y.N. Liang, S.Z. Li, Y.B. Jin, W. Jin, S. Li, Wear **198**, 236 (1996). [https://doi.org/10.1016/0043-1648\(96\)06989-X](https://doi.org/10.1016/0043-1648(96)06989-X)

Publisher's Note Springer Nature remains neutral with regard to jurisdictional claims in published maps and institutional affiliations.

Springer Nature or its licensor (e.g. a society or other partner) holds exclusive rights to this article under a publishing agreement with the author(s) or other rightsholder(s); author self-archiving of the accepted manuscript version of this article is solely governed by the terms of such publishing agreement and applicable law.